

# Sheltering effect of punched steel plate sand fences for controlling blown sand hazards along the Golmud–Korla Railway: Field observation and numerical simulation studies

ZHANG Kai<sup>1,2\*</sup>, TIAN Jianjin<sup>1</sup>, QU Jianjun<sup>2</sup>, ZHAO Liming<sup>1</sup>, LI Sheng<sup>1</sup>

<sup>1</sup> College of Civil Engineering, Lanzhou Jiaotong University, Lanzhou 730000, China;

<sup>2</sup> Key Laboratory of Desert and Desertification, Northwest Institute of Eco-Environment and Resources, Chinese Academy of Sciences, Lanzhou 730000, China

**Abstract:** Sand fences made of punched steel plate (PSP) have recently been applied to control wind-blown sand in desertified and Gobi areas due to their strong wind resistance and convenient *in situ* construction. However, few studies have assessed the protective effect of PSP sand fences, especially through field observations. This study analyzes the effects of double-row PSP sand fences on wind and sand resistance using field observations and a computational fluid dynamics (CFD) numerical simulation. The results of field observations showed that the average windproof efficiencies of the first-row and second-row sand fences were 79.8% and 70.8%, respectively. Moreover, the average windproof efficiencies of the numerical simulation behind the first-row and second-row sand fences were 89.8% and 81.1%, respectively. The sand-resistance efficiency of the double-row PSP sand fences was 65.4%. Sand deposition occurred close to the first-row sand fence; however, there was relatively little sand on the leeward side of the second-row sand fence. The length of sand accumulation near PSP sand fences obtained by numerical simulation was basically consistent with that through field observations, indicating that field observations combined with numerical simulation can provide insight into the complex wind-blown sand field over PSP sand fences. This study indicates that the protection efficiency of the double-row PSP sand fences is sufficient for effective control of sand hazards associated with extremely strong wind in the Gobi areas. The output of this work is expected to improve the future application of PSP sand fences.

**Keywords:** punched steel plate; sheltering effect; field observations; computational fluid dynamics numerical simulation; windproof efficiency

**Citation:** ZHANG Kai, TIAN Jianjin, QU Jianjun, ZHAO Liming, LI Sheng. 2022. Sheltering effect of punched steel plate sand fences for controlling blown sand hazards along the Golmud–Korla Railway: Field observation and numerical simulation studies. *Journal of Arid Land*, 14(6): 604–619. <https://doi.org/10.1007/s40333-022-0019-7>

## 1 Introduction

Researcher divided sand-control measures into solidification, resistance, dredging, and diversion categories according to their functions and properties (Bruno and Fransos, 2015; Li and Sherman, 2015; Horvat et al., 2021). Among these, sand-resistant engineering measures primarily include high vertical sand barriers, sand fences, and forest belts (Hewes, 1981; Vercauteren et al., 2006).

\*Corresponding author: ZHANG Kai (E-mail: zhangkai0212@yeah.net)

Received 2022-03-09; revised 2022-05-30; accepted 2022-06-08

© Xinjiang Institute of Ecology and Geography, Chinese Academy of Sciences, Science Press and Springer-Verlag GmbH Germany, part of Springer Nature 2022

Sand-resistant engineering is generally deployed at the front of sand protection system to increase resistance to wind-blown sand by reducing wind velocity and blocking, and intercepting sand on the windward side of sand fence (Snyder and Pinet, 1981; Sherman and Nordstrom, 1994; Miller et al., 2001; Grafals-Soto and Nordstrom, 2009; Jackson and Nordstrom, 2011).

In recent years, a variety of sand-resistant materials (polyethylene (PE) mesh, nylon mesh, plug-in concrete walls, sleeper-style windscreens, etc.) suitable for the aeolian environment have been applied in sand-control engineering, especially in China (Yang et al., 2020); and much experience pertaining to sand control under different conditions has been attained. Specifically, sand fences made of PE and nylon mesh are more sensitive to wind velocity, and are generally used in low-wind energy areas where velocity is lower than 10 m/s (Yang et al., 2020). Wang et al. (1999) conducted a wind tunnel test to assess the protection efficiency of white nylon mesh and ultraviolet (UV)-resistant mesh sand fences on the Tarim Desert Highway, China. They revealed that the porosity of white nylon mesh sand fence was 64%, and wind velocity on the leeward side of the fence was approximately 20% lower than the initial wind velocity, while the porosity of UV-resistant nylon mesh sand fence was 58%. Qu et al. (2001) found that wind velocity on the leeward side of a sand fence was 30% lower than the initial wind velocity, and sand deposition efficiency of a nylon mesh sand fence with a porosity of 40%–45% was 50% under extreme wind velocity (24 m/s). In high wind energy areas, especially in high-altitude plateaus, sand fences such as plug-in concrete walls and sleeper-style windscreens are often used for railway protection from wind-blown sand (Bruno et al., 2018a, b). Yang et al. (2020) studied the sand control effects of different types of sand-resistant measures using wind tunnel tests. They found that plug-in concrete walls and sleeper-style windscreens are the least sensitive to wind velocity, and the wind-proof efficiency of sand fences is the highest under high wind velocity (Huang et al., 2019). However, due to the large pore spacing of plug-in concrete walls and sleeper-style windscreens, sand accumulation on the railway line on the lee side of the windshield wall remained serious, indicating the low sand-resistance efficiency of the windshield (Huang et al., 2019). In addition, plug-in concrete walls and sleeper-style windscreens have many disadvantages, such as inconvenient transport, tedious construction, and poor economic efficiency. In contrast, punched steel plate (PSP) sand fences proposed in recent years are made of a new type of sand-resistant material, and can be conveniently and quickly installed during the construction process. Wang et al. (2018) tested the protection provided by PSP sand fences using wind tunnel experiments, and found that windproof and sand-resistance efficiencies of the single-row and double-row PSP sand fences were greater than 70% and 80%, respectively, indicating that PSP sand fences could effectively control sand hazards caused by extremely strong wind in the Gobi areas. However, to date, only wind tunnel tests have been conducted to assess the protective effect of PSP sand fences, and verification through field observation data is lacking. Due to space limitations, wind tunnel tests hardly produce the correct geometry, kinematics, and dynamics simultaneously (Li and Sherman, 2015). Therefore, the results of wind and sand flow around sand fences are quite different from those in the field (Hagen et al., 1981).

The Golmud–Korla Railway has a total length of 1214 km, and extends from the city of Golmud in Qinghai Province in the east to the city of Korla in Xinjiang Uygur Autonomous Region in the west. The third railway out of Xinjiang, the Golmud–Korla Railway improves the railway network in western China, and has great significance for promoting the development of the region around the line by strengthening national unity and enhancing the convenience of transportation from the mainland of China to central Asia and southern Europe (Zhang et al., 2019a). The location of the railway line in the Qaidam and Tarim basins primarily on the leeward side of strong wind velocity with stable wind direction for long periods and seasonality. Moreover, the underlying surface on both sides of the railway is primarily sandy gravel, which easily releases wind-blown sand under strong wind. Consequently, control of wind-blown sand over the Gobi areas is a key technology for railway safety (Bruno et al., 2018c; Tan et al., 2020). The geographical and environmental characteristics along the Qinghai Province of the Golmud–Korla

Railway make the use of plants for sand fixation unfeasible (Zhang et al., 2019b). Thus, sand-resistant measures are primarily utilized for railway protection, and double-row PSP sand fences are installed in the Zhongzaohuo area along the railway line. However, an evaluation of the shelter efficiency of the double-row PSP sand fences, particularly through *in situ* field observations and numerical simulation, has not been reported in the literature. Due to the complexity of wind field, observations can only measure the average wind velocity and sand flux density at limited locations, and hardly reveal the turbulence characteristics around the entire sand fence (Li and Sherman, 2015; Bruno et al., 2018a). Field observations combined with numerical simulations can provide greater insights into the complex wind field than wind tunnel test (Horvat et al., 2020).

In this study, an evaluation of the protection effect of the double-row PSP sand fences laid in the Golmud–Korla Railway was conducted by field observation to address their windproof and sand-resistance efficiencies. In addition, the computational fluid dynamics (CFD) numerical simulation method was used to verify characteristics of the flow field on the leeside of the double-row PSP sand fences. Overall, this study provides favorable and theoretical support for the design and improvement of the railway sand-control system, which is of great significance for the safe operation of railway.

## 2 Study area

Figure 1a shows the annual sand-driving wind rose in the study area (the height of weather station was 6 m above the ground). Sand-driving wind velocity in the region around the Golmud–Korla Railway is approximately 6.0 m/s at a height of 6 m above the ground (Zhang et al., 2019a). The dominant wind directions in this region were WNW (west-north-west), W (west), and NW (north-west), accounting for 56.1% of the annual sand-driving wind frequency. The secondary wind directions were N (north) and NW (north-west), accounting for 12.6%. The maximum wind velocity was 21.2 m/s, with an instantaneous value of 23.1 m/s. The maximum wind velocity in 2018 occurred to the NW (north-west). In 2018, the annual frequency of sand-driving wind in the region was 12.2%; the maximum monthly sand-driving wind frequency was 21.3% in May; and the minimum was 4.1% in December. The sand-driving wind frequency was greater than the average from February to July in 2018 (Fig. 1b).

The annual drift potential (DP) of the region was calculated using the method proposed by Fryberger (1979). According to the calculation, the annual DP of the region was 452.07 VU, which indicates a high wind energy environment. The resultant drift potential (RDP) was 328.20 VU; the resultant drift direction (RDD) was 105.56°, and the RDP/DP (the variation rate of DP) was 0.726, indicating a bimodal wind condition (Fig. 1c).

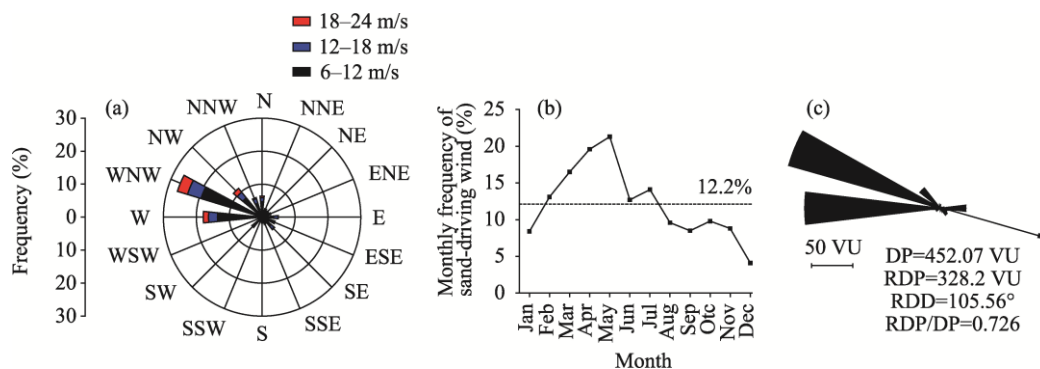


**Fig. 1** Aeolian environment of study area. (a), annual sand-driving wind rose; (b), monthly frequency of sand-driving wind; (c), annual drift potential. DP, drift potential; RDP, resultant drift potential; VU, vector units; RDD, resultant drift direction.

Crescent dunes near the sand-control system were important sources of railway sand hazards in the region. Gobi wind-blown sand forms under the action of westerly winds, causing sand accumulation on the railbed. Seasonal rivers distributed across the region carry abundant sediment during the wet season, some of which settles to form a sand bed. Moreover, water erosion can destroy the gravel cover of the underlying surface. In the dry season, the wind velocity exceeds the sand-driving velocity, thus, railway wind-sand damage occurs easily.

Double-row PSP sand fences are installed on the windward side of the railway subgrade in suit. The height of the fences is 2 m, and the porosity of sand fences is 50% provided by the railway designer. The distance between the two rows of fences is 40 m, and the fence length is 2 km.

### 3 Methods

#### 3.1 Field observation

HOBO U30 anemometers (U30-NRC, Onset, USA) were established at different heights. Additionally, 1-m-high portable sand traps were installed at 40 m (20.0 H, where H is the height of the sand fence) and 1 m (0.5 H) in the upwind direction of the first-row sand fence; at 1 m (0.5 H), 20 m (10.0 H), and 39 m (19.5 H, 0.5 H before the second-row PSP sand fence) on the leeward side of the first-row sand fence; and at 1 m (0.5 H), 20 m (10.0 H), and 40 m (20.0 H) on the leeward side of the second-row PSP sand fence (Fig. 2). The heights of the HOBO anemometers were 0.2, 0.5, 1.0, 1.5, and 2.0 m; and the height of wind direction vane was 2 m. The acquisition frequency of wind velocity and wind direction was 0.1 Hz, and the recording interval was 1 min. The 1-m-high sand traps were a portable flat-mouth sand collector with an opening size of 2 cm×2 cm. Fifty sand collectors were used. The efficiency of the sand traps was between 72% and 87%. The wind-blown sand field was observed on 16 May, 2018 during the westerly wind transport process. The dominant wind direction in this region was westerly wind. The average angle between the observed wind-blown sand and the trend of system section was 92°, and they were basically vertical. The wind velocity at a height of 2 m above the ground was 10.3 m/s, and the instantaneous maximum wind velocity was 17.5 m/s.

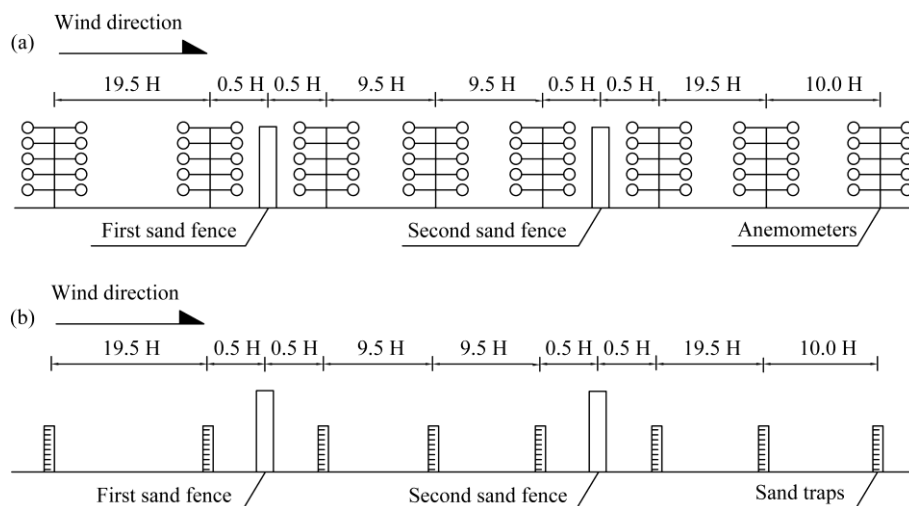


**Fig. 2** Field observation made on double-row PSP sand fences. (a), cross-section diagram of the anemometers; (b), cross-section diagram of the sand traps. PSP, punched steel plate, H, the height of the sand fence, which is 2 m.

#### 3.2 Simulation method

##### 3.2.1 Mathematical models

The simulation was conducted using the Reynolds number average Navier-Stokes equation, which

is suitable for simulating the time-average flow characteristics of long-term morphological dynamics around railways. Since the SST (shear-stress-transport)  $k$ - $\omega$  turbulence model has been proved to be an accurate model of the wind-sand solid barrier (Horvat et al., 2020), it is selected for the current study. All simulations were performed under steady-state conditions, and the inlet airflow was turbulent, incompressible, and separated.

The entire governing equation expressed in Einstein symbols and Cartesian coordinates is as follow (Menter et al., 2003; Bruno et al., 2018c; Horvat et al., 2021):

$$\frac{\partial u_i}{\partial X_i} = 0, \quad (1)$$

$$u_j \frac{\partial u_i}{\partial X_j} = -\frac{1}{\rho} \frac{\partial p}{\partial X_i} + \frac{\partial}{\partial X_j} \left[ \nu + \nu_t \frac{\partial u_i}{\partial X_j} + \frac{\partial u_j}{\partial X_i} \right], \quad (2)$$

$$u_j \frac{\partial k}{\partial X_j} = \frac{\partial}{\partial X_j} \left[ (\sigma_k \nu_t + \nu) \frac{\partial k}{\partial X_j} \right] + P_k - \beta^* k \omega, \quad (3)$$

$$u_j \frac{\partial \omega}{\partial X_j} = \frac{\partial}{\partial X_j} \left[ (\sigma_\omega \nu_t + \nu) \frac{\partial \omega}{\partial X_j} \right] + C_{\omega 1} \frac{\omega}{k} P_k - C_{\omega 2} \omega^2 + (1 - F_1) \frac{2\sigma_{\omega 2}}{\omega} \frac{\partial k}{\partial X_i} \frac{\partial \omega}{\partial X_i}, \quad (4)$$

where  $u_i$  is the averaged velocity in the  $i$  direction (m/s);  $X_i$  is the  $i$  direction along the  $X$  axis;  $u_j$  is the averaged velocity in the  $j$  direction (m/s);  $X_j$  is the  $j$  direction along the  $X$  axis;  $P$  is the averaged pressure (Pa);  $\rho$  is the air density (kg/m<sup>3</sup>);  $\nu$  is the air kinematic viscosity (m<sup>2</sup>/s);  $k$  is the turbulent kinetic energy (m<sup>2</sup>/s<sup>2</sup>);  $\omega$  is the specific dissipation rate (m<sup>2</sup>/s<sup>2</sup>); and  $\nu_t$  is the turbulent kinematic viscosity (m<sup>2</sup>/s). The kinetic energy production term  $\tilde{P}_k$  is modeled by introducing a limiter to prevent the build-up of turbulence in stagnation regions:

$$P_k = \min(P_k, 10\beta^* k \omega); \quad P_k \approx \nu_t \frac{\partial u_i}{\partial x_j} + \frac{\partial u_j}{\partial x_i} \frac{\partial u_i}{\partial x_j}. \quad (5)$$

For the sake of conciseness, the definition of the blending function  $F_1$  and the values of the model main constants  $\beta^*$ ,  $\sigma_k$ ,  $\sigma_\omega$ ,  $\sigma_{\omega 2}$ ,  $C_{\omega 1}$  and  $C_{\omega 2}$  are omitted herein. The indices can be found in detail from Menter et al. (2003).

In order to reflect the influence of the roughness elements on the ground wind field, the SST  $k$ - $\omega$  model needs to supplement the sand-grain roughness wall function. This supplement is based on the equivalent sand grain roughness length ( $K_s$ ) and roughness constant ( $C_s$ ). Rough wall modification with roughness height is determined as  $K_s = 9.793 z_0 / C_s$ , where  $C_s = 0.5$  is the roughness constant; and  $z_0$  is the aerodynamic roughness length (m).

A 3D model was used for numerical simulation, which was built by using AutoCAD software. The calculation domain included the flat ground on the windward and leeward of the sand fence, as well as the sand fence itself. The length and height of the computational domain of the fluid were  $L_x = 100.0 H$  and  $L_z = 20.0 H$ , respectively (Fig. 3). We set the size  $L_y = 10.0 H$  according to the method of Horvat et al. (2021). The distances of the entire computational domain were 20.0 H and 40.0 H from the sand fences in the windward and leeward directions, respectively, which were sufficiently large ( $>15.0 H$ ) to avoid influences of boundary conditions on the results. The geometric model for numerical simulation was established with a PSP sand fence at a height of 2 m. The thickness of the sand fence was 2 mm, and the length was 20 m. The holes on the sand fences were elliptical, with the short side of 1.0 cm and the long side of 1.5 cm. Therefore, there were approximately  $42 \times 10^3$  ellipses in a row of sand fence, and the ellipses were evenly distributed on the sand fence. The porosity of 50% was defined as the percentage of the area of the holes to the total area of the fence; and PSP sand fences were spaced at 40-m intervals.

The medium type of the model was designated as "fluid", the inlet wall surface was defined as "inlet", the outlet wall surface was defined as "outflow", the upper wall surface and the left- and right-wall surfaces were defined as "symmetry", and PSP sand fences and the lower

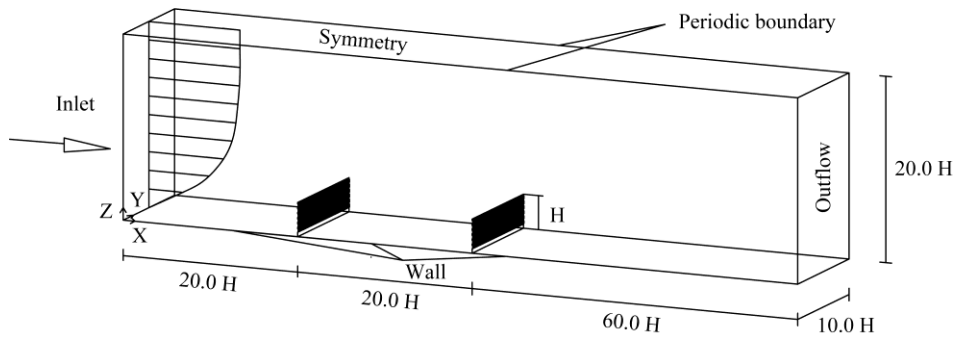


**Fig. 3** Schematic diagram of the model of computational domain and boundary conditions.  $H$ , the height of the sand fence, which is 2 m.

wall surface of the model were defined as "wall". The inlet wind velocity profile was obtained by Equation 5; and the reference wind velocity at a specified height of 2 m was 10.3 m/s, which was equal to the measured wind data. To simplify the calculation, we judged the wind profile to be similar to the wind profile on the open natural ground (Wakes et al., 2010; Jackson et al., 2011). The aerodynamic roughness length  $z_0$  and friction wind velocity were 0.87 mm and 0.497 m/s, respectively, which were estimated from the wind profile of the reference anemometer array using the method of Bauer et al. (1992). We calculated the inlet boundary conditions for  $k$  and  $\omega$  according to the following formula for the assumption of a balanced boundary layer (Liu et al., 2011):

$$U_Z = \frac{u_*}{\kappa} \ln \frac{z + z_0}{z_0}, \quad (6)$$

$$k = 1.5(u_{\text{avg}} I)^2, \quad (7)$$

$$\omega = k^{0.5} / C_\mu^{0.25} / l, \quad (8)$$

where  $U_Z$  is the wind velocity at height  $Z$  (m/s);  $u_*$  is the friction wind velocity (shear wind velocity; m/s);  $\kappa$  is the Karman constant, which is generally 0.4 (Richards and Hoxey, 1993; Santiago and Martin, 2005);  $z$  is the height above the ground (m); and  $z_0$  is the aerodynamic roughness length, which generally refers to the height at which the velocity is 0 (m). The values of the model main constants  $u_{\text{avg}}$ ,  $I$ ,  $l$ ,  $C_\mu^{0.25}$  are omitted herein, which can be referenced from Ansys (2019).

### 3.2.2 Simulation method

Ansys Workbench software was used to generate a grid for the governing transport equations. Because of the complexity of geometric models, this study used a hybrid grid scheme with a hexahedral grid, which was easily adapted to the geometric models (Fig. 4). In the simulation, the center of the adjacent wall unit was placed in the logarithmic layer and that the logarithmic layer was valid. The wall function requirement on dimensionless wall unit  $30 < n^+ < 200$  (Blocken et al., 2007). The grid convergence index method was used for grid sensitivity analysis and discrete error estimation (Celik et al., 2008; Tan et al., 2016). An important integral parameter for the horizontal wind velocity at 2 m above the ground was studied as the simulation objective. We chose three meshes for analysis, and took three values of  $n_w$ , namely  $n_w = 0.00125 H$ ,  $0.0015 H$ , and  $0.003 H$ , where  $n_w$  is the height of the adjacent wall cell (m). The overall linearity factor of coarsening and refinement was 1.56 that could ensure the normal operation of the computer and found the appropriate number of grids. The selected grids were  $8.82 \times 10^6$  (grid 1),  $4.91 \times 10^6$  (grid 2), and  $2.26 \times 10^6$  (grid 3). Table 1 shows the results of the discretization error of horizontal velocity. The numerical uncertainty of fine-grid solution of horizontal velocity was 1.21% in these sites. The solution error in grid 2 was within an acceptable range.



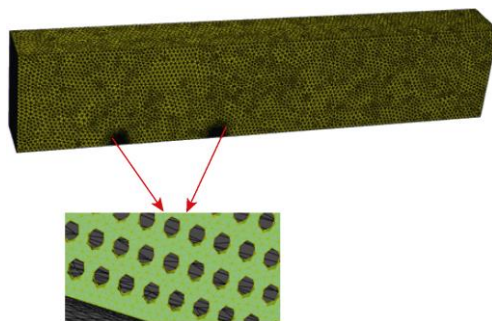


**Fig. 4** Simulated mesh and the mesh near the hole of sand fence

**Table 1** Calculated local order accuracy ( $p$ ) and fine-grid convergence indices ( $GCI_{21}^{fine}$ ) for horizontal velocities

| Index                 | $H_X=50$ m | $H_X=60$ m | $H_X=100$ m | $H_X=120$ m |
|-----------------------|------------|------------|-------------|-------------|
| $u_{grid1}$ (m/s)     | 6.231      | 15.326     | 3.636       | 6.132       |
| $u_{grid2}$ (m/s)     | 5.672      | 14.676     | 3.521       | 5.643       |
| $u_{grid3}$ (m/s)     | 6.303      | 15.441     | 3.754       | 6.198       |
| $p$                   | 1.850      | 2.090      | 1.110       | 1.790       |
| $GCI_{21}^{fine}$ (%) | 1.21       | 0.65       | 2.36        | 1.42        |

Note:  $u$  is the horizontal velocity on the  $X$ -axis at a height of 2 m above the surface;  $H_X$  is the distance from the entrance.

A steady-state solver was used for the Fluent simulation. The finite volume element method was used to calculate the flow field numerically, the second-order upwind discrete scheme was adopted for the momentum, and the first-order upwind formula was adopted for  $k$  and  $\omega$  (Lima et al., 2020). The flow field was initialized by the value set by the inlet boundary condition. The convergence criterion of the scaled residual error was set to  $10^{-6}$  for all the variables and the continuity equation; and the calculation was aggregated except for the continuity equation (when the remaining ratio of the continuity equation reached  $10^{-4}$ ). Additional iterations were performed until the residual ratio of all variables, and the continuity equation did not further reduce (Yang et al., 2009).

### 3.2.3 Wind and sand characteristics

The incoming wind flow used in simulations can reflect real environment in the study site. The aerodynamic roughness length  $z_0$  and friction wind velocity were 0.87 mm and 0.497 m/s, respectively, which were estimated from the wind profile of the reference anemometer array using the method reported by Bauer et al. (1992). The adopted particle size of the sand was 0.1 mm, which was the result measured in the laboratory after we took the sand on site (Zhang et al., 2021), and was in line with the particle size range of Raffaele et al. (2016). Meanwhile, the inhomogeneity in the horizontal direction was obvious to the airflow in the watershed. The solution to this problem was mainly to measure without setting up sand fences. We mainly used the same method as Liu et al (2011) to measure incident flow and approach flow. In this study, the "incident" position is the place in an empty domain where the model (at the first-row sand fence) is to be settled in the corresponding simulation. The "inlet" position is the place at the entrance (20.0 H before the first-row sand fence). The "approach" flow is measured before the disturbed area of the model (10.0 H before the first-row sand fence). It can be seen from Figure 1 that the wind speed profiles at different locations in the basin were consistent, and the  $k$ ,  $\omega$ , and  $p$  profiles were also the same (Fig. 5).

### 3.3 Data processing

First, the wind velocities at different measuring points and different heights of the sand-control system cross section were measured by the multi-gradient HOB0 anemometers, and the

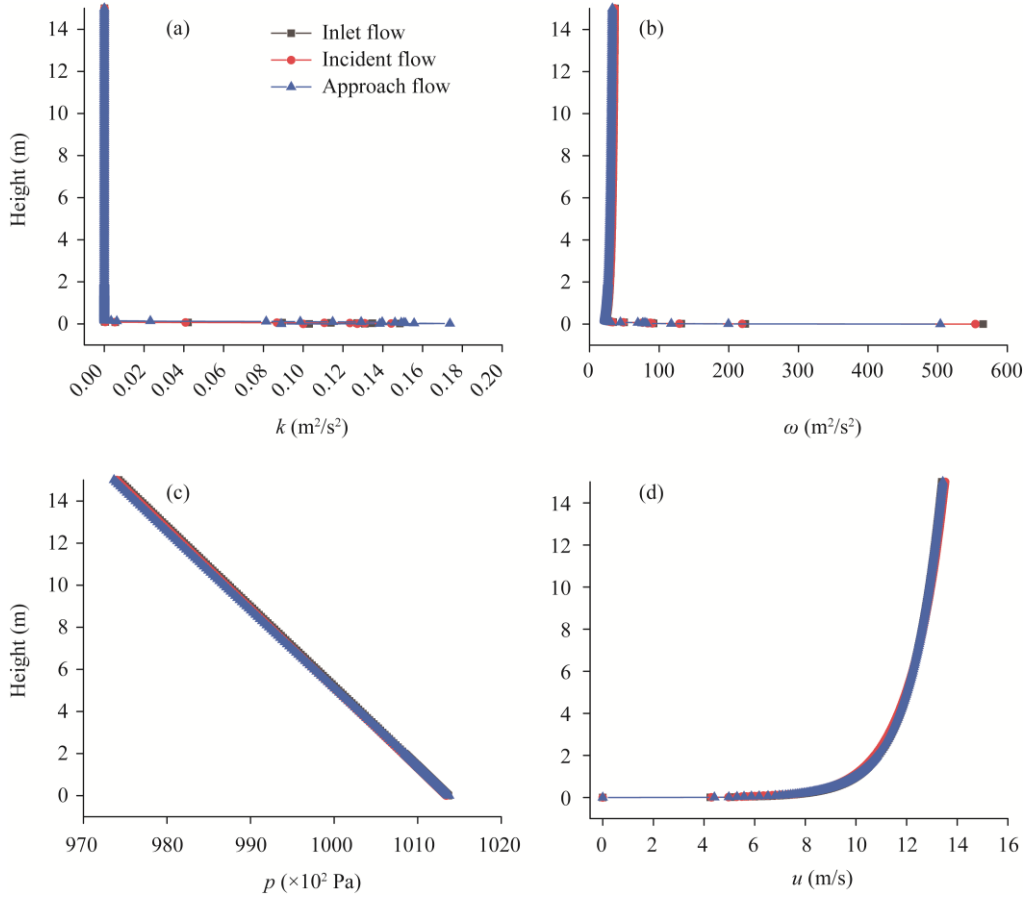


**Fig. 5** Inlet, approach, and incident flows in empty computational domains. (a), vertical profiles of the turbulent kinetic energy ( $k$ ); (b), vertical profiles of the specific dissipation rate ( $\omega$ ); (c), vertical profiles of the absolute pressure ( $p$ ); (d), vertical profiles of the mean wind velocity ( $u$ ).

windproof efficiency of the sand-control system (i.e., the attenuation percentage of the wind velocity of the flow after it entered the sand-control system) was calculated. The calculation formula of the windproof efficiency of the sand-control system follows (Wang et al., 2018; Zhang et al., 2021):

$$\eta_w = \frac{u_{0Z} - |u_{1Z}|}{u_{0Z}} \times 100\%, \quad (9)$$

where  $\eta_w$  is the windproof efficiency of the sand-control system, with values ranging from 0 to 1;  $u_{0Z}$  is the wind velocity of the peripheral control point at height  $Z$  (m/s); and  $u_{1Z}$  is the wind velocity of the internal measurement point at height  $Z$  (m/s). The change of wind velocity only refers to the change of magnitude, and has nothing to do with direction.

Additionally, the sand flux density at different measuring points changes with the attenuation of the sand-control system, that is, the sand-resistance efficiency (Wang et al., 2018), which was calculated as follows:

$$\eta_Q = \frac{(Q_Z - Q_{Z1})}{Q_Z} \times 100\%, \quad (10)$$

where  $\eta_Q$  is the sand-resistance efficiency of the sand-control system;  $Q_Z$  is the sand flux density within the height of 1 m at the peripheral control point of the sand-control system ( $\text{g}/(\text{m}^2 \cdot \text{s})$ ); and  $Q_{Z1}$  is the sand flux density within the height of 1 m at the internal measurement point of the sand-control system ( $\text{g}/(\text{m}^2 \cdot \text{s})$ ).



## 4 Results

### 4.1 Field observation

#### 4.1.1 Variation of windproof efficiency

Figure 6 shows the variation of wind velocity around the double-row sand fences under field test conditions. It can be seen from the figure that when the airflow passed through the double-row PSP sand fences, the airflow velocity decreased after the first-row sand fence, and the airflow velocity was significantly reduced. The airflow velocity was still lower than the original airflow velocity before the second-row sand fence. After passing through the second-row sand fence, the airflow velocity decreased again. As the distance from the second-row sand fence increased, the wind velocity gradually recovered.

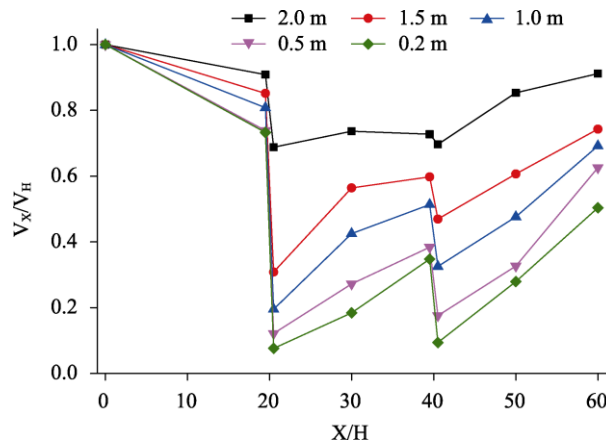


**Fig. 6** Wind velocity variation around double-row sand fences.  $X/H$  is the ratio of the distance in the  $X$  direction to  $H$ ; and  $V_x/V_H$  is ratio of the velocity in the  $X$  direction to the velocity of the fence height  $H$ .

Equation 8 was used to calculate the windproof efficiency at different wind velocities. For an average wind velocity of 10.3 m/s, the windproof efficiencies at heights of 0.2 and 0.5 m and at a distance of 0.5  $H$  behind the first-row sand fence were 92.4% and 87.9%, respectively. At 10.0  $H$  from the first-row sand fence, the windproof efficiencies decreased to 81.6% and 72.8%, respectively, indicating recovered airflow. The windproof efficiencies at heights of 0.2 and 0.5 m at 0.5  $H$  behind the second-row sand fence increased to 90.6% and 82.4%, respectively. The windproof efficiencies at 10.0  $H$  and 20.0  $H$  behind the second-row sand fence decreased to 72.1% and 67.3%, and 49.6% and 37.4%, respectively. Therefore, a significant wind velocity reduction zone behind PSP sand fences reduced the carrying capacity of wind-blown sand. The sand particles settled to form a sand deposit, and PSP sand fences played a protective role.

#### 4.1.2 Variation of sand-resistance efficiency

Figure 7a shows the relationship curves between the sand flux density at different heights and the sand fence, where the sand flux density is defined as the amount of sediment passing through a unit area in unit time ( $\text{g}/(\text{m}^2 \cdot \text{s})$ ). The sand flux density decreased with increasing height before the first-row sand fence at 20.0  $H$ . Nonlinear regression analysis of the experimental data showed that the sand flux density followed a decreasing exponential function with height. The following exponential decay function was used for the relationship between sand flux density and height:

$$Q_z = C + A e^{(-BZ)}, \quad (11)$$

where  $A$ ,  $B$  and  $C$  are all constants; and  $Z$  is the height from the ground (m).

However, for wind-blown sand passing through PSP sand fences, the sand flux density no longer followed the declining exponential function, and the sand flux density decreased significantly behind the sand fence. For wind velocity on the leeward side of the sand fence that is

less than the sand-driving wind velocity, the transmission between the surrounding winds is very weak; therefore, most sand grains settle around the sand fence, thus stopping the saltation process of surface sand grains.

The sand flux density was calculated to analyze the variation along the sand-control system, and to evaluate the sand-resistance efficiency of the sand-control system (Fig. 7b). For an average wind velocity of 10.3 m/s, the average sand flux density at the control point outside the sand-control system during observation period was 14.3 g/(m<sup>2</sup>·s). The sand flux density decreased to 8.8 and 9.6 g/(m<sup>2</sup>·s) at 0.5 H and 10.0 H behind the first-row sand fence, respectively. After passing through the second-row sand fence, the average sand flux density at 0.5 H and 10.0 H behind the sand fence further decreased to 6.5 and 5.6 g/(m<sup>2</sup>·s), respectively. Finally, the average sand flux density at 20.0 H behind the second-row sand fence was 5.0 g/(m<sup>2</sup>·s). The average sand flux density leeward the double-row PSP sand fences continued to decrease, especially leeward the second-row sand fence.

The sand-resistance efficiency was calculated by Equation 10 to further analyze the protection benefit of the sand-control system (Fig. 7c). The results showed that the sand-resistance efficiency was negative at 0.5 H before the first-row sand fence; thus, the mass of sand grains collected at this location increased, and sand grains accumulated in front of the first-row sand fence. The sand-resistance efficiencies at 0.5 H and 10.0 H behind the first-row sand fence were 38.8% and 33.1%, respectively. The sand-resistance efficiencies at 10.0 H and 20.0 H behind the second-row sand fence were 61.2% and 65.4%, respectively. Hence, the sand-control system of double-row sand fences had a good sand-resistance effect, and blocked most of wind-blown sand.

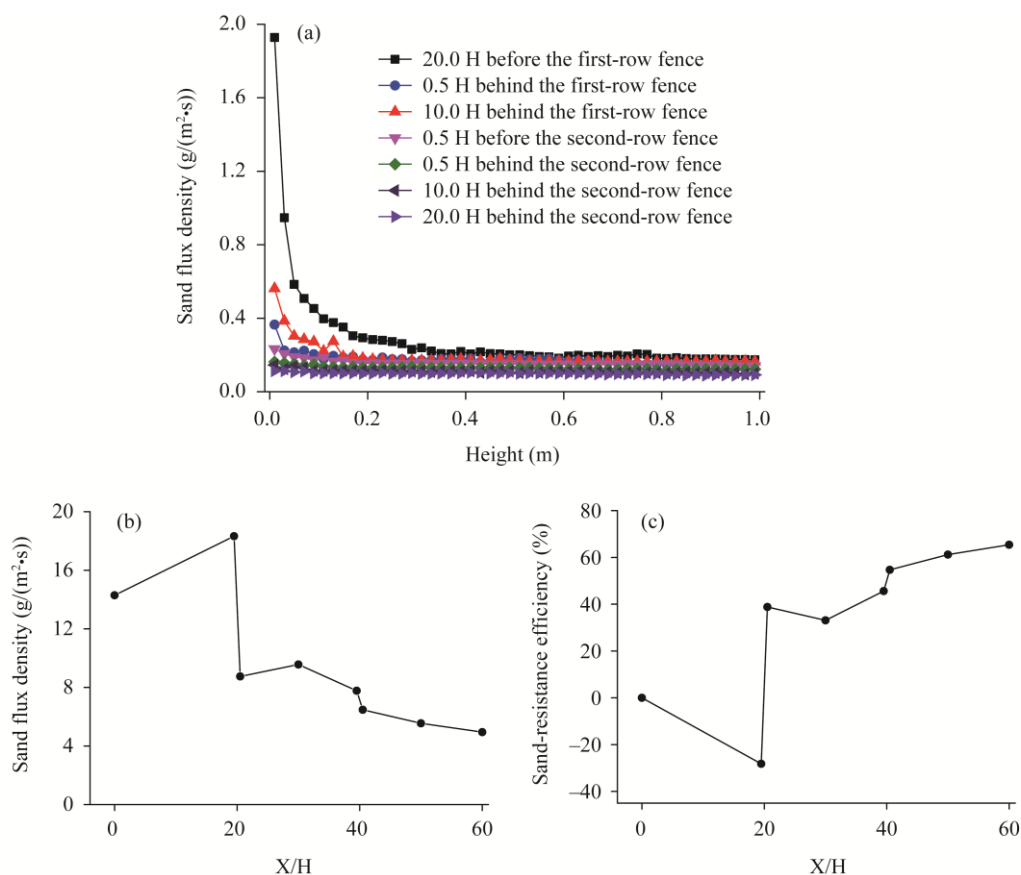


**Fig. 7** (a), sand flux density around the double-row PSP sand fences for a wind velocity of 10.3 m/s; (b), variation of sand flux density along the sand-control system; (c), variation of sand-resistance efficiency along the sand-control system. X/H is the ratio of the distance in the X direction to H.

## 4.2 Numerical simulation

### 4.2.1 Flow test in the field

A deceleration zone formed in front of the first-row sand fence, and the wind velocity decreased as the airflow passed through the double-row PSP sand fences (Fig. 8a). The upper airflow lifted to form an acceleration zone as the airflow passed through the first-row sand fence. The airflow below the first-row sand fence was hindered by the formation of a large elliptic backflow zone behind the first-row sand fence, and the direction of the airflow changed. The airflow velocity was relatively low in the backflow zone but decreased before the second-row sand fence (Fig. 8b). After passing through the second-row sand fence, the upper airflow steadily increased, and the lower airflow formed a small backflow zone behind the second-row sand fence. The airflow continued advancing. After passing beyond the second-row sand fence, the wind velocity gradually recovered.

The wind velocity of 10.3 m/s decreased rapidly at 5.0 H from the front of the first-row sand fence (Fig. 8c). After passing the first-row sand fence, a backflow zone generated behind the sand fence due to the irregular airflow and the wind velocity was negative (opposite the direction of incoming wind velocity). The length of the backflow zone reached 12.8 H, and the maximum velocity in the recirculation zone was 3.9 m/s. In the backflow zone, sand grains settled quickly

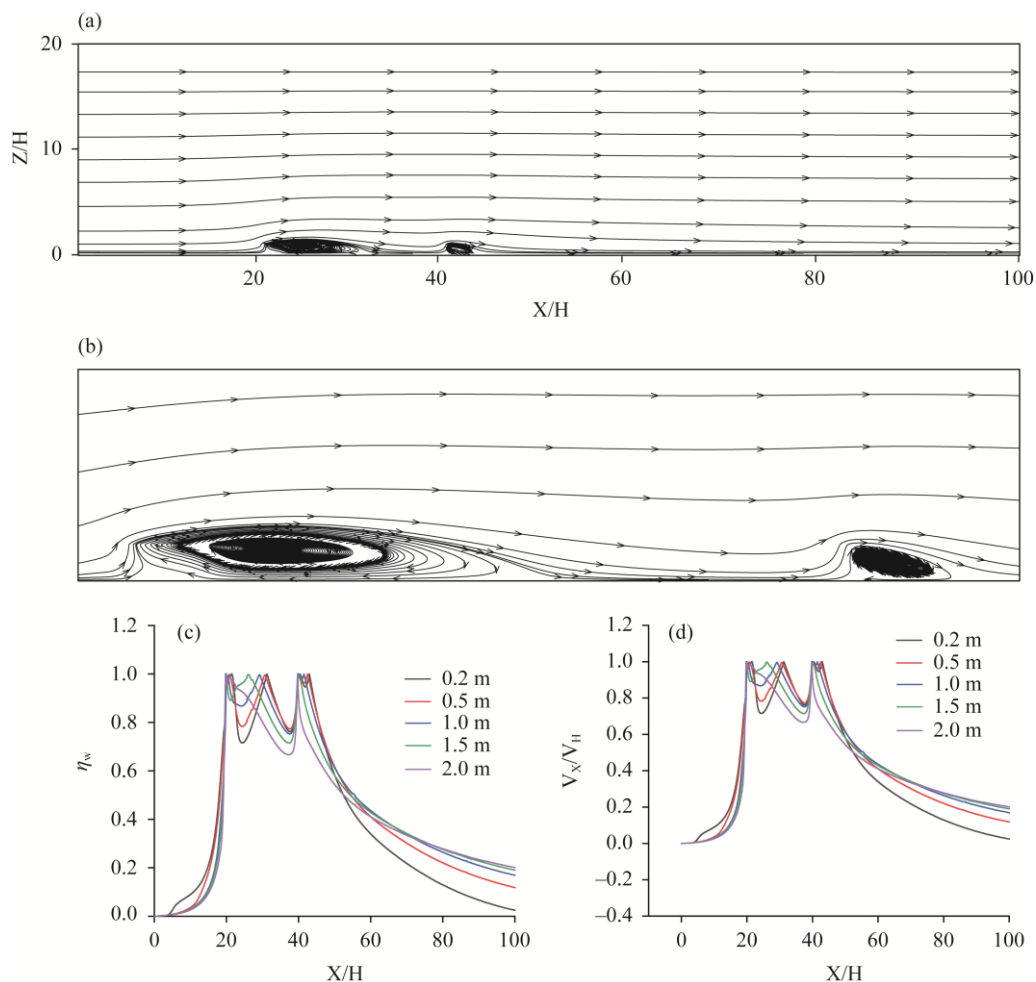


**Fig. 8** (a), Overall diagram of the flow field distribution of the double-row PSP sand fences ( $Z/H$  is the ratio of the distance along the  $Z$  direction to  $H$ ); (b), normalized diagram of horizontal velocity distribution diagram of double-row PSP sand fences; (c), horizontal velocity distribution diagram of the double-row PSP sand fences; (d), windproof efficiency of double-row PSP sand fences.  $X/H$  is the ratio of the distance in the  $X$  direction to  $H$ .

because of the counter-clockwise airflow and accumulated behind the first-row sand fence. The backflow zone was affected by the airflow passing through the holes of the first-row sand fence, and gradually disappeared. The velocity increased to a maximum value at approximately 2.5 H in front of the second-row sand fence. The maximum velocities at 0.2 and 1.5 m above the ground were 2.5 and 3.0 m/s, respectively, and decreased rapidly under the influence of the second-row sand fence. A small backflow zone formed beyond the second-row sand fence. The length of the backflow zone was approximately 4.9 H, and the maximum value of  $V_x/V_H$  in the recirculation zone was 0.06. Finally, the wind velocity gradually returned to its initial state. Within the height range of the double-row PSP sand fences, the wind velocity variation showed a W-shaped distribution (i.e., decreasing, increasing, and returning to the initial velocity along the flow direction).

#### 4.2.2 Windproof efficiency

We used Equation 9 to calculate the windproof efficiency of sand fences (Fig. 8d). The windproof efficiency gradually increased on the windward side of the first-row sand fence as the airflow passed through the double-row PSP sand fences. The change in windproof efficiency was relatively complex for airflow between the first-row and second-row sand fences but remained above 60%. The windproof efficiency decreased significantly with increasing distance beyond 10.0 H on the leeward side of the second-row sand fence. Sand movement is a sand transportation phenomenon in which more than 70% of moving sand is concentrated within 0.3 m of the ground. Therefore, the windproof efficiency of the double-row PSP sand fences was studied at a height of 0.2 m above the ground. For a wind velocity of 10.3 m/s, the windproof efficiencies at 0.5 H, 10.0 H, and 19.5 H beyond the first-row sand fence were 99.2%, 72.5%, and 97.6%, respectively; the efficiencies were 99.1%, 96.1%, and 48.2% at 0.5 H, 10.0 H, and 20.0 H beyond the second-row sand fence, respectively.

## 5 Discussion

### 5.1 Sand-resistance effect

Sand fences are generally placed at the foremost edge of a protection system with the principal purposes of increasing the resistance to wind-blown sand, reducing wind velocity, and blocking and intercepting drifting sand. In the field test, the windproof and sand-resistance efficiencies at 0.5 H before the first-row sand fence are 24.0% and 28.2%, respectively, with a difference of 4.2%. The windproof and sand sand-resistance efficiency at 0.5 H before the second-row sand fence are 45.6% and 58.5%, respectively, with a difference of 12.9%. The windproof and sand-resistance efficiency at 10.0 H after the second-row sand fence are 61.2% and 63.9%, respectively, with a difference of 2.7%. The average windproof efficiencies behind the first-row and second-row sand fences were 79.8% and 70.8%, respectively. The maximum sand-resistance efficiency behind the second-row sand fence was 65.4%.

Wang et al. (2018) conducted a wind tunnel test to assess the windproof efficiency and sand flux density of double-row PSP sand fences, and concluded that the maximum average windproof efficiency and the maximum sand-resistance efficiency behind the second-row sand fence were 87.5% and 84.5%, respectively. The maximum windproof efficiency and the maximum sand-resistance efficiency results of the wind tunnel test were 16.7% and 19.1% higher than the field test results, respectively.

Previous studies show that the saltation of sand grains changes significantly in time and space, even on a relatively flat quicksand surface (Zhang et al., 2010; Li et al., 2015). Gares et al. (1996) found that the transportation of sand grains changed by 25% within a 15-min interval. Jackson et al. (2006) found that the transportation of sand grains may exceed 1.5 times the variability within 5 m. In a field experiment, the inherent variability in sand transport and the turbulence around the sand fence improved the variability of sand-resistance efficiency (Wilson and Yee, 2003). Changes in wind direction during sand transport further increase the uncertainty of the sand flux

density, and variations in the angle between the airflow and the sand fence change the shear force of the sand grain surface on the leeward side of the sand fence. However, studying multi-row sand fences in a wind tunnel is difficult, because the size of sand grains, the length of saltation, and the aperture size of the sand fences are limited after scaling the sand fence. The differences in the saltation height and length scale of sand grains in the wind tunnel versus in the field create additional complexity.

## 5.2 Comparison between the numerical simulation and field observation

The numerical simulation results showed that the airflow passed through PSP sand fences and that the air velocity substantially decreased under the influence of the fences, which formed a deceleration zone on the windward side and a backflow zone on the leeward side of PSP sand fences. Gillies et al. (2017) summarized the airflow behind a porous sand fence, which formed a new boundary layer at the top edge. The backflow zone developed along the wind direction, and the new boundary layer returned to the equilibrium condition at a distance generally much greater than 10.0 H from the leeward side of the sand fence. Airflow was ejected when passing through an acceleration zone above the leeward side of the sand fence (Wilson et al., 1990). Thus, a circular or upright backflow zone was formed, and the direction of the airflow close to the surface was opposite to that of the incoming wind velocity.

By comparing Figures 7 and 9, it can be seen that the wind velocity gradually decreased after the first-row and second-row sand fences. Taking 20.0 H behind the second-row sand fence as an example, the wind velocities at the heights of 0.2, 0.5, 1.0, and 1.5 m from the ground were 0.50, 0.63, 0.69, and 0.74 times of the inlet wind velocity in the field test. In the numerical simulation, the wind velocities at the heights of 0.2, 0.5, 1.0, and 1.5 m from the ground were 0.52, 0.49, 0.51, and 0.55 times of the inlet wind velocity. The average wind velocity of the field test was 0.64 times of the inlet wind velocity in the field test, and the average wind velocity of the numerical simulation was 0.52 times of the inlet wind velocity in the numerical simulation, and the former was 1.2 times that of the latter.

The average windproof efficiency of the numerical simulation behind the first-row and second-row sand fences were 89.8% and 81.1%, respectively. The average windproof efficiencies of the first-row and the second-row sand fences differed by 10% and 10.4% from the numerical simulation results, respectively. In the numerical simulation process, referring to the work of Horvat et al. (2021), the ground shear force ( $\tau_i$ ) is proportional to the sand particle size, so the value of  $\tau_i$  is 0.045 Pa.  $\tau$  is defined as the surface shear stress by wind flow. When  $\tau/\tau_i$  is smaller than -1, it represents backward erosion; when it is in the range of [-1, 1], it represents sedimentation; and when it is larger than 1, it represents positive erosion (abbreviated as erosion). Figure 9 depicts the simulated deposition and erosion around the fence. It can be seen from the figure that the length of the sand on the windward side of the first-row sand fence is 1.0 H, and the length of the sand on the leeward side of the fence is 4.0 H. There is also sand accumulation between the first-row and the second-row sand fences with a length of 6.0 H, and a sand accumulation of 10.3 H on the leeward side of the first-row sand fence. Hotta and Horikawa (1991) showed that, for a porosity percentage of 50%, the leeward length of the *in situ* measured sand pile is 10.0 H (The fence heights were 0.9 and 1.2 m). The ratio of sand accumulation length to fence height after the first-row sand fence is consistent with the field measurement data of

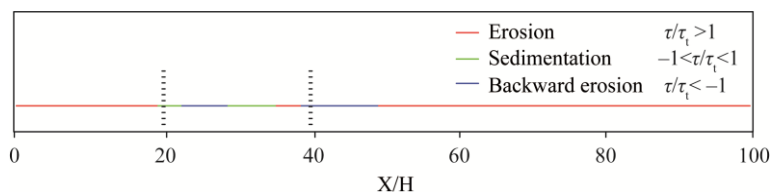


**Fig. 9** Deposition and erosion around the fence.  $X/H$  is the ratio of the distance in the  $X$  direction to  $H$ ,  $\tau$ , surface shear stress by wind flow;  $\tau_i$ , ground shear force.



Hotta and Horikawa (1991). In terms of the pattern and length of deposition, most sand grains pass through the first-row sand fence and pile on the leeward side. Sand deposition occurs close to the first-row sand fence. However, there is relatively little sand on the leeward side of the second-row sand fence (Fig. 10). The length of the sand on the windward side of the first-row sand fence in the field ranges from  $1.8 H$  to  $2.9 H$ , and the length of the sand on the leeward side of the first-row sand fence ranges from  $5.7 H$  to  $12.6 H$ ; the length of the sand on the windward side of the second-row sand fence ranges from  $1.2 H$  to  $2.5 H$ , and the length of the sand on the leeward side of the first-row sand fence ranges from  $3.6 H$  to  $8.5 H$ . Thus, the length of the deposited sand in the numerical simulation is consistent with the results of the field test. Due to the influence of the first-row sand fence, the sand velocity drops to the threshold velocity for sand movement, causing most of the sand particles accumulate behind the first-row sand fence.

This study simulated the interaction between wind-blown sand and sand fences based on the integration of field observation data in the Gobi areas. The velocity around the double-row PSP sand fences was basically consistent with the field observation data. Moreover, numerical simulation provided more detailed data.

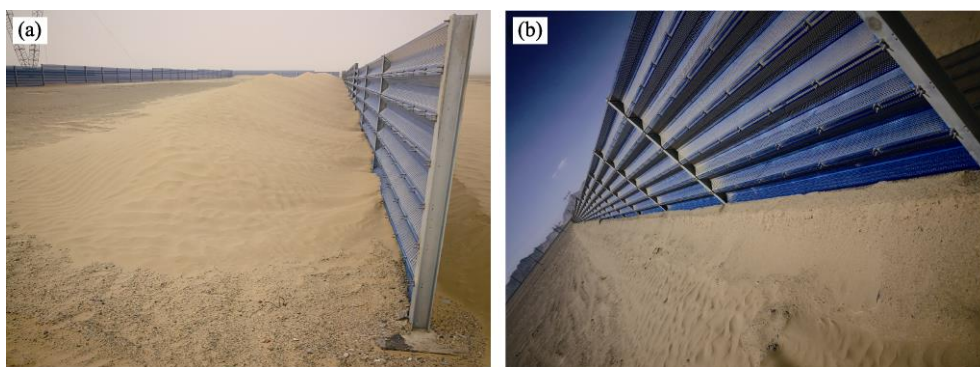


**Fig. 10** Double-row PSP sand fences on study area. (a), first-row sand fence; (b), second-row sand fence.

## 6 Conclusions

When the wind-sand flow passed through the double-row PSP sand fences, the wind velocity decreased and formed a vortex after the first-row and second-row sand fences, and the wind velocity gradually recovered to the initial wind velocity as it moved away from the sand fence. The double-row perforated board sand fences played a good windproof effect in the prevention and control of sand hazards in the Gobi areas. The windproof efficiency of the double-row sand fences can reach more than 80.0%. The sand transport flux no longer followed the exponential decreasing function, and the sand transport flux decreased significantly after the sand fences. Away from the sand fences, the sediment flux and height followed an exponentially decreasing function. The maximum sand-resistance efficiency of the double-row sand fences was 65.4%, the sand accumulation was mainly distributed after the first-row sand fence, and the sand accumulation length of the sand fence was approximately  $10.0 H$ . In the field observation, the locations and number of monitoring points are limited by the characteristics of the field environment, number of instruments, wind velocity, and wind direction. Based on the integration of field system observation data, the CFD simulation method can be used to simulate the interaction between wind-blown sand and sand fences to obtain more detailed data in the Gobi areas.

## Acknowledgements

This research was funded by the Fellowship of the China Postdoctoral Science Foundation (2021M703466), the Basic Research Innovation Group Project of Gansu Province, China (21JR7RA347), and the Natural Science



Foundation of Gansu Province, China (20JR10RA231). The authors express appreciation for the anonymous reviewers and the editor, who helped improve the quality of this paper.

## References

- Bauer B O, Sherman D J, Wolcott J F. 1992. Sources of uncertainty in shear stress and roughness length estimates derived from velocity profiles. *The Professional Geographer*, 44(4): 453–464.
- Blocken B, Stathopoulos T, Carmeliet J. 2007. CFD simulation of the atmospheric boundary layer: wall function problems. *Atmospheric Environment*, 41(2): 238–252.
- Bruno L, Fransos D. 2015. Sand transverse dune aerodynamic: 3D coherent flow structures from a computational study. *Journal of Wind Engineering and Industrial Aerodynamics*, 147: 291–301.
- Bruno L, Horvat M, Raffaele L. 2018a. Windblown sand along railway infrastructures: A review of challenges and mitigation measures. *Journal of Wind Engineering and Industrial Aerodynamics*, 177: 340–365.
- Bruno L, Coste N, Fransos D, et al. 2018b. Shield for sand: an innovative barrier for windblown sand mitigation. *Recent Patents on Engineering*, 12(3): 237–246.
- Bruno L, Fransos D, Giudice A L. 2018c. Solid barriers for windblown sand mitigation: aerodynamic behavior and conceptual design guidelines. *Journal of Wind Engineering and Industrial Aerodynamics*, 173: 79–90.
- Celik I B, Ghia U, Roache P J, et al. 2008. Procedure for estimation and reporting of uncertainty due to discretization in CFD applications. *Journal of Fluid Mechanics*, 130(7): 078001, doi: 10.1115/1.2960953.
- Fryberger S G. 1979. Dune forms and wind regime. In: McKee E D. *A Study of Global Sand Seas*, USGS Professional Paper 1052. Washington DC: USGS and NASA: 137–169.
- Gares P A, Davidson-Arnott R G D, Bauer B O, et al. 1996. Alongshore variations in aeolian sediment transport: Carrick Finn Strand, Ireland. *Journal of Coastal Research*, 12: 673–682.
- Gillies J A, Etyemezian V, Nikolich G, et al. 2017. Effectiveness of an array of porous fences to reduce sand flux: Oceano Dunes, Oceano CA. *Journal of Wind Engineering and Industrial Aerodynamics*, 168: 247–259.
- Grafals-Soto R, Nordstrom K. 2009. Sand fences in the coastal zone: intended and unintended effects. *Environmental Management*, 44: 420–429.
- Hagen L J, Skidmore E L, Miller P L, et al. 1981. Simulation of effect of wind barriers on airflow. *Transactions of the ASAE*, 24: 1002–1008.
- Hewes L. 1981. Early fencing on the western margin of the prairie. *Annals of the Association of American Geographers*, 71(4): 499–527.
- Horvat M, Bruno L, Khri S, et al. 2020. Aerodynamic shape optimization of barriers for windblown sand mitigation using CFD analysis. *Journal of Wind Engineering and Industrial Aerodynamics*, 197: 104058, doi: 10.1016/j.jweia.2020.104058.
- Horvat M, Bruno L, Khri S. 2021. CWE study of wind flow around railways: Effects of embankment and track system on sand sedimentation. *Journal of Wind Engineering and Industrial Aerodynamics*, 208: 104476, doi: 10.1016/j.jweia.2021.104476.
- Hotta S, Horikawa K. 1991. Function of sand fence placed in front of embankment. *Coastal Engineering*, 2: 2754–2767.
- Huang N, Gong K, Xu B, et al. 2019. Investigations into the law of sand particle accumulation over railway subgrade with wind-break wall. *The European Physical Journal E*, 42(11): 145, doi: 10.1140/epje/i2019-11910-0.
- Jackson D W T, Beyers J H M, Lynch K, et al. 2011. Investigation of three-dimensional wind flow behaviour over coastal dune morphology under offshore winds using Computational Fluid Dynamics (CFD) and ultrasonic anemometry. *Earth Surface Processes and Landforms*, 36(8): 1113–1124.
- Jackson N L, Sherman D J, Hesp P A, et al. 2006. Small-scale spatial variations in aeolian sediment transport on a fine-sand beach. *Journal of Coastal Research*, 39(12): 379–383.
- Jackson N L, Nordstrom K F. 2011. Aeolian sediment transport and landforms in managed coastal systems: A review. *Aeolian Research*, 3(2): 181–196.
- Li B L, Sherman D J. 2015. Aerodynamics and morphodynamics of sand fences: A review. *Aeolian Research*, 17: 33–48.
- Lima I A, Parteli E J R, Shao Y P, et al. 2020. CFD simulation of the wind field over a terrain with sand fences: Critical spacing for the wind shear velocity. *Aeolian Research*, 43:100574, doi: 10.1016/j.aeolia.2020.100574.
- Liu B L, Qu J J, Zhang W M, et al. 2011. Numerical simulation of wind flow over transverse and pyramid dunes. *Journal of Wind Engineering and Industrial Aerodynamics*, 99(8): 879–888.
- Menter F R, Kuntz M, Langtry R. 2003. Ten years of industrial experience with the SST turbulence model. In: Hanjali C K, Nagano Y, Tummers J. *Turbulence Heat and Mass Transfer 4: Proceedings of the Fourth International Symposium on Turbulence, Heat and Mass Transfer*, Antalya, Turkey, 12–17.
- Miller D L, Thetford M, Yager L. 2001. Evaluation of sand fence and vegetation for dune building following overwash by

- Hurricane Opal on Santa Rosa Island, Florida. *Journal of Coastal Research*, 17(4): 936–948.
- Qu J J, Liu X W, Lei J Q, et al. 2001. Simulation experiments on sand-arresting effect of nylon net fence in wind tunnel. *Journal of Desert Research*, 21(3): 276–280. (in Chinese)
- Raffaele L, Bruno L, Pellerey F, et al. 2016. Windblown sand saltation: a statistical approach to fluid threshold shear velocity. *Aeolian Research*, 23: 79–91.
- Richards P J, Hoxey R P. 1993. Appropriate boundary conditions for computational wind engineering models using the  $k-\epsilon$  turbulence model. *Journal of Wind Engineering and Industrial Aerodynamics*, 46–47: 145–153.
- Santiago J L, Martin F. 2005. Modelling the air flow in symmetric and asymmetric street canyons. *International Journal of Environment and Pollution*, 25(1–4): 145–154.
- Sherman D J, Nordstrom K F. 1994. Hazards of wind-blown sand and coastal sand drifts: A review. *Journal of Coastal Research*, 12: 263–275.
- Snyder M R, Pinet P R. 1981. Dune construction using two multiple sand-fence configurations: implications regarding protection of eastern Long Island's south shore. *Northeastern Geology*, 3: 225–229.
- Tan L H, Zhang W M, Bian K, et al. 2016. Numerical simulation of three-dimensional wind flow patterns over a star dune. *Journal of Wind Engineering and Industrial Aerodynamics*, 159: 1–8.
- Tan L H, An Z S, Zhang K, et al. 2020. Intermittent aeolian saltation over a Gobi surface: threshold, saltation layer height, and high-frequency variability. *JGR Earth Surface*, 125(1): e2019JF005329, doi: 10.1029/2019JF005329.
- Tennekes H. 1973. The logarithmic wind profile. *Journal of Atmospheric Sciences*, 30(2): 234–238.
- Vercauteren K C, Lavelle M J, Hygnstrom S. 2006. Fences and deer-damage management: A review of designs and efficacy. *Wildlife Society Bulletin*, 34: 191–200.
- Wakes S J, Maegli T, Dickinson K J, et al. 2010. Numerical modelling of wind flow over a complex topography. *Environmental Model and Software*, 25: 237–247.
- Wang T, Qu J J, Ling Y Q, et al. 2018. Shelter effect efficacy of sand fences: A comparison of systems in a wind tunnel. *Aeolian Research*, 30: 32–40.
- Wang X M, Chen G T, Han Z W, et al. 1999. The benefit of the prevention system along the desert highway in Tarim Basin. *Journal of Desert Research*, 19(2): 120–127. (in Chinese)
- Wilson J D, Swaters G E, Ustina F. 1990. A perturbation analysis of turbulent flow through a porous barrier. *Quarterly Journal of the Royal Meteorological Society*, 116(494): 989–1004.
- Wilson J D, Yee E. 2003. Calculation of winds disturbed by an array of fences. *Agricultural and Forest Meteorology*, 115: 31–50.
- Yang Y, Gu M, Chen S Q, et al. 2009. New inflow boundary conditions for modelling the neutral equilibrium atmospheric boundary layer in computational wind engineering. *Journal of Wind Engineering and Industrial Aerodynamics*, 97(2): 88–95.
- Yang Y H, Xue C X, Shi L, et al. 2020. Sand resistance rate of retaining wall along the Qinghai-Tibet Railway. *Journal of Desert Research*, 40(1): 173–178. (in Chinese)
- Zhang K, Wang Q C, Yang Z J, et al. 2019a. Research on numerical simulation on wind protection benefits of HDPE panels with high vertical sand barrier in the newly-built Golmud–Korla Railway. *Journal of China Railway Society*, 41(3): 169–175. (in Chinese)
- Zhang K, Yang Z J, Wang Q C, et al. 2019b. Relationship between porosity and effective protection distance of HDPE board sand barrier on Golmud–Korla Railway. *China Railway Science*, 40(5): 16–21. (in Chinese)
- Zhang K, Zhao P W, Zhao J C, et al. 2021. Protective effect of multi-row HDPE board sand fences: A wind tunnel study. *International Soil and Water Conservation*, 9(1): 103–115.
- Zhang N, Kang J H, Lee R J. 2010. Wind tunnel observation on the effect of a porous wind fence on shelter of saltating sand particles. *Geomorphology*, 120(3–4): 224–232.